Published for SISSA by Springer

Received: *August 3, 2023*
Accepted: *September 30, 2023*
Published: *October 12, 2023*

Scalarized Kerr-Newman black holes

Guangzhou Guo,[a,b] **Peng Wang,**[a] **Houwen Wu**[a,c] **and Haitang Yang**[a]

[a]*Center for Theoretical Physics, College of Physics, Sichuan University, Chengdu, 610064, China*
[b]*Department of Physics, Southern University of Science and Technology, Shenzhen, 518055, China*
[c]*Department of Applied Mathematics and Theoretical Physics, University of Cambridge, Wilberforce Road, Cambridge, CB3 0WA, U.K.*

E-mail: guogz@sustech.edu.cn, pengw@scu.edu.cn, hw598@damtp.cam.ac.uk, hyanga@scu.edu.cn

Abstract: In this paper, we construct scalarized rotating black holes within the framework of Einstein-Maxwell-scalar models. These models incorporate non-minimal couplings that can induce tachyonic instabilities, leading to the spontaneous scalarization of Kerr-Newman (KN) black holes. By exploring the domain of existence, we observe that the presence of scalarized KN black holes is suppressed by the black hole spin, with a maximum spin threshold beyond which scalarized solutions cease to exist. Intriguingly, we find that in specific parameter regimes, scalarized KN black holes can exhibit the presence of two unstable and one stable light rings on the equatorial plane, manifesting in both prograde and retrograde directions.

Keywords: Black Holes, Classical Theories of Gravity

ArXiv ePrint: 2307.12210v2

https://doi.org/10.1007/JHEP10(2023)076

JHEP10(2023)076

Contents

JHEP10(2023)076

1 Introduction

In the past decade, the groundbreaking detections of gravitational waves from binary black hole mergers by LIGO and Virgo have opened up new avenues for testing general relativity in the strong field regime [1]. During the ringdown phase of a black hole merger, the emitted gravitational waves can be described by a superposition of quasinormal modes [2]. Extracting these quasinormal modes from the observed gravitational wave signals allows us to determine the properties of the remnant black hole, e.g., its mass, charge, and angular momentum, thus providing a promising tool to test the validity of the Kerr hypothesis [3, 4]. Furthermore, a significant breakthrough in the field of black hole observation was achieved with the recent release of images of the supermassive black holes M87* and Sgr A* by the Event Horizon Telescope (EHT) collaboration [5–16]. While the detections of gravitational waves and the observed black hole images align well with the predictions of Kerr black holes, it is worth noting that the limitations in observational resolution leave room for exploration of alternative theories and black hole mimics.

The no-hair theorem asserts that black holes are characterized exclusively by their mass, electric charge and angular momentum [17–19]. However, various models have been formulated that give rise to hairy black holes endowed with additional degrees of freedom, thereby serving as counterexamples to the no-hair theorem [20–29]. One prominent counterexample is spontaneous scalarization, which typically occurs in models featuring non-minimal couplings between scalar fields and other fields. These coupling terms serve as sources that destabilize scalar-free black hole solutions and give rise to the formation of scalarized hairy black holes.

Initially explored in the context of scalar-tensor models for neutron stars, spontaneous scalarization was found when scalar fields are coupled to the Ricci curvature [30]. It was demonstrated that a coexistence region exists where scalar-free and scalarized neutron star solutions compete energetically, with the scalarized solutions often exhibiting a preference. Subsequently, it was discovered that spontaneous scalarization can also manifest in black hole spacetime in scalar-tensor models, provided that black holes are coupled to non-linear electrodynamics [31, 32] or surrounded by non-conformally invariant matter [33, 34]. More recently, the phenomenon of spontaneous scalarization has been investigated in extended Scalar-Tensor-Gauss-Bonnet (eSTGB) gravity [35–41]. In eSTGB models, the scalar field is non-minimally coupled to the Gauss-Bonnet curvature correction in the gravitational sector, which can induce the formation of spinning scalarized black holes [39, 40]. However, the presence of non-linear curvature terms in the eSTGB models brings numerical challenges in solving the evolution equations.

To gain a deeper understanding of the dynamical evolution leading to the formation of scalarized black holes, a technically simpler class of models called Einstein-Maxwell-scalar (EMS) models has been proposed [42]. These models incorporate non-minimal couplings between the scalar and Maxwell fields, which introduce tachyonic instabilities capable of triggering spontaneous scalarization. In [42], fully non-linear numerical simulations in spherical symmetry demonstrated the evolution of Reissner-Nordström (RN) black holes into scalarized RN black holes. Subsequent investigations of the EMS models have yielded a wealth of research findings, e.g., different non-minimal coupling functions [43–45], massive and self-interacting scalar fields [46, 47], horizonless reflecting stars [48], stability analysis of scalarized black holes [49–53], higher dimensional scalar-tensor models [54], quasinormal modes of scalarized black holes [55, 56], two U(1) fields [57], quasitopological electromagnetism [58], topology and spacetime structure influences [59], scalarized black hole solutions in the dS/AdS spacetime [60–64], and dynamical scalarization and descalarization [65–67].

Remarkably, scalarized RN black holes have been discovered to exhibit the presence of multiple photon spheres outside the event horizon in specific parameter regimes [68]. Subsequent investigations have focused on the optical appearances of various phenomena in the background of scalarized RN black holes, e.g., accretion disks [68, 69], luminous celestial spheres [70] and infalling stars [71]. These studies have revealed that the existence of an additional photon sphere significantly increases the flux of observed accretion disk images, generates triple higher-order images of a luminous celestial sphere, and gives rise to an additional cascade of flashes from an infalling star. Furthermore, the presence of multiple photon spheres in a spacetime also suggests the existence of long-lived modes that may render the spacetime unstable [72–76]. Specifically, it has been shown that the existence of multiple photon spheres outside the event horizon can induce superradiance instabilities for charged scalar perturbations [77]. For a more detailed analysis of black holes with multiple photon spheres, we refer readers to the work [78].

Recently, it has been reported that tachyonic instabilities around Kerr-Newman (KN) black holes can lead to unstable scalar perturbations in the EMS model, indicating the existence of scalarized rotating black holes [79]. The aim of this paper is twofold: first, to numerically construct scalarized rotating black hole solutions in the EMS model; and

JHEP10(2023)076

second, to investigate whether scalarized rotating black holes possess multiple light rings. The rest of the paper is organized as follows. In section 2, we introduce the construction of scalarized KN black holes in the EMS model and discuss light rings on the equatorial plane. Subsequently, we present the numerical results for the scalarized black hole solutions and their light ring structure in section 3. We conclude our main results and provide discussions in section 4. We set $G = c = 4\pi\epsilon_0 = 1$ throughout this paper.

2 Einstein-Maxwell-scalar model

In the EMS model, where a scalar field is non-minimally coupled to electromagnetism, the background spacetime can become destabilized through a tachyonic instability, leading to the phenomenon of spontaneous scalarization in black holes. The corresponding action is described as

$$S = \frac{1}{16\pi}\int d^4x\sqrt{-g}\left[R - 2\partial_\mu\phi\partial^\mu\phi - f\left(\phi\right)F^{\mu\nu}F_{\mu\nu}\right], \tag{2.1}$$

where ϕ is the scalar field, $F_{\mu\nu} = \partial_\mu A_\nu - \partial_\nu A_\mu$ denotes the electromagnetic field strength tensor, and A_μ represents the electromagnetic field. To accommodate scalar-free black hole solutions with $\phi = 0$, the coupling function $f\left(\phi\right)$ must satisfy $f'\left(0\right) \equiv df\left(\phi\right)/d\phi|_{\phi=0} = 0$. In this paper, we focus on the specific exponential coupling function denoted as

$$f\left(\phi\right) = e^{\alpha\phi^2}, \tag{2.2}$$

where the coupling constant $\alpha > 0$. It has been observed that this exponential coupling function (2.2) has the capability to induce tachyonic instabilities in scalar perturbations, ultimately resulting in spontaneous scalarization in non-rotating charged black holes [42, 43]. In this section, we present the numerical construction of scalarized KN black holes in the EMS model and investigate null circular geodesics (i.e., light rings) within these scalarized KN black holes.

2.1 Tachyonic instability

In the scalar-free background, represented by KN black holes, the scalar perturbation $\delta\phi$ is governed by the equation

$$\left(\Box - \mu_{\text{eff}}^2\right)\delta\phi = 0, \tag{2.3}$$

where $\mu_{\text{eff}}^2 = \alpha F^{\mu\nu}F_{\mu\nu}/2$. In the Boyer-Linquist coordinates, the KN black hole can be described by

$$\begin{aligned} ds^2 = & -\frac{\left(\triangle - a^2\sin^2\theta\right)}{\Sigma}dt^2 - 2a\sin^2\theta\frac{\left(r^2+a^2-\triangle\right)}{\Sigma}dtd\phi \\ & + \left(\frac{\left(r^2+a^2\right)^2 - \triangle a^2\sin^2\theta}{\Sigma}\right)\sin^2\theta d\phi^2 + \frac{\Sigma}{\triangle} + \Sigma d\theta^2, \\ A = & \frac{Qr\left(dt - a\sin^2\theta d\phi\right)}{\Sigma}, \end{aligned} \tag{2.4}$$

where

$$\Sigma = r^2 + a^2r^2\cos^2\theta \text{ and } \triangle = r^2 - 2Mr + a^2, \tag{2.5}$$

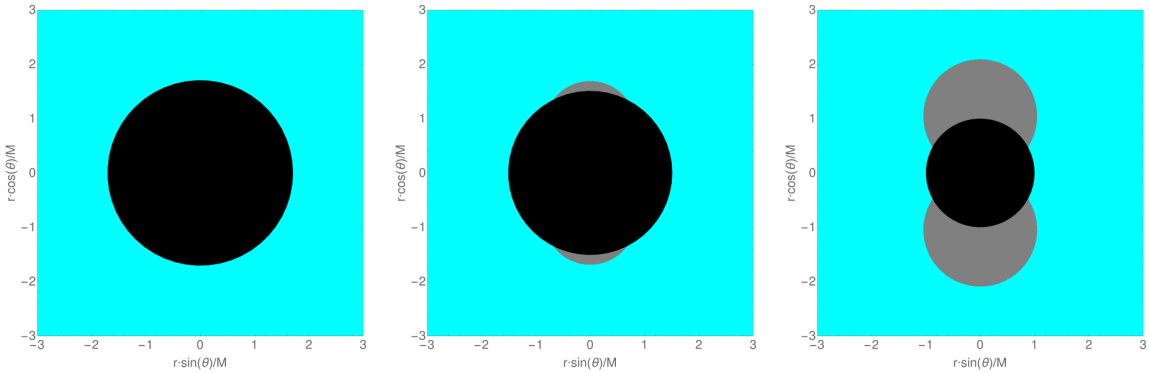

Figure 1. In the $r\sin\theta/M - r\cos\theta/M$ plane, gray regions denote areas where $\mu_{\rm eff}^2 > 0$, while blue regions indicate $\mu_{\rm eff}^2 < 0$. KN black holes are represented by the black regions. The left, middle, and right panels correspond to $a/M = 0.500$, 0.700 and 0.866, respectively. As black hole spin increases, the gray regions with positive $\mu_{\rm eff}^2$ gradually emerge and subsequently expand, demonstrating the alleviation of tachyonic instabilities.

Q is the black hole charge, and a represents the ratio of black hole angular momentum J to mass M (i.e., $a \equiv J/M$). Note that KN black holes become extremal when $a^2 = M^2 - Q^2$. Moreover, the effective mass square in eq. (2.3) can be expressed as

$$\mu_{\rm eff}^2 = -\frac{\alpha Q^2\left(r^4 - 6a^2r^2\cos^2\theta + a^4\cos^4\theta\right)}{\left(r^2 + a^2\cos^2\theta\right)^4}. \tag{2.6}$$

Notably, tachyonic instabilities arise in the presence of a negative effective mass square $\mu_{\rm eff}^2 < 0$, which could induce scalarized black holes from the scalar-free background.

In figure 1, we exhibit the regions characterized by the sign of the effective mass square $\mu_{\rm eff}^2$ in the $r\sin\theta/M - r\cos\theta/M$ plane. These regions are displayed for a range of values of a/M while maintaining $Q/M = 0.5$. Note that the corresponding extremal value of a/M is 0.866. In addition, the $r\sin\theta/M - r\cos\theta/M$ plane can be viewed as the vertical plane aligned with the symmetry axis of black holes. The shaded gray areas within the plots represent regions where $\mu_{\rm eff}^2 > 0$. These regions are absent when the black hole spin is insufficiently large. Following their emergence, the gray regions expand as the parameter a/M increases, suggesting that higher black hole spin alleviates tachyonic instabilities. As a result, it raises the possibility that, under a sufficiently large black hole spin, spontaneous scalarization within KN black holes may cease to occur. When restricted to the equatorial plane, the effective mass square reduces to $\mu_{\rm eff}^2 = -\alpha Q^2/r^4$, which coincides with the RN black hole case [42, 63]. In the RN black hole background, it has demonstrated that the tachyonic instabilities near the black hole event horizon can be strong enough to trigger spontaneous scalarization. By analogy, we expect similar tachyonic instabilities to induce scalarized KN black holes from the KN black hole background.

To investigate the onset of spontaneous scalarization in KN black holes, we need to solve the linear perturbation equation (2.3) for zero-modes $\delta\phi(r,\theta)$. The presence of these zero-modes often indicates the existence of scalarized black hole solutions. Specifically, the zero-modes correspond to bifurcation points in the parameter space, marking the onset of

JHEP10(2023)076

scalarized KN black holes. In the latter part of this section, we will discuss the numerical scheme employed to find the zero-modes $\delta\phi\,(r,\theta)$.

2.2 Rotating black hole solution

The equations of motion for the metric field $g_{\mu\nu}$, the scalar field ϕ and the electromagnetic field A_μ can be obtained by varying the action (2.1), yielding

$$\begin{aligned} R_{\mu\nu}-\frac{1}{2}Rg_{\mu\nu} &= 2T_{\mu\nu}, \\ \Box\phi-\frac{\alpha}{2}\phi e^{\alpha\phi^2}F^{\mu\nu}F_{\mu\nu} &= 0, \\ \partial_\mu\left(\sqrt{-g}e^{\alpha\phi^2}F^{\mu\nu}\right) &= 0, \end{aligned} \tag{2.7}$$

where the energy-momentum tensor $T_{\mu\nu}$ is expressed as

$$T_{\mu\nu}=\partial_\mu\phi\partial_\nu\phi-\frac{1}{2}g_{\mu\nu}\left(\partial\phi\right)^2+e^{\alpha\phi^2}\left(F_{\mu\rho}F_\nu{}^\rho-\frac{1}{4}g_{\mu\nu}F_{\rho\sigma}F^{\rho\sigma}\right). \tag{2.8}$$

Following [40, 80, 81], we consider stationary, axisymmetric and asymptotically-flat black hole solutions with the generic ansatz

$$\begin{aligned} ds^2 &= -e^{2F_0}Ndt^2+e^{2F_1}\left(\frac{dr^2}{N}+r^2d\theta^2\right)+e^{2F_2}r^2\sin^2\theta\left(d\varphi^2-\frac{W}{r^2}dt\right)^2, \\ A_\mu dx^\mu &= \left(A_t-A_\varphi\frac{W}{r^2}\sin\theta\right)dt+A_\varphi\sin\theta d\varphi \text{ and } \phi=\phi\left(r,\theta\right), \end{aligned} \tag{2.9}$$

where $N\equiv 1-r_H/r$, and r_H is the black hole horizon. Here, the metric functions F_0, F_1, F_2, W, A_t and A_φ are assumed to depend solely on the coordinates r and θ. By substituting the ansatz (2.9) into eq. (2.7), we derive a set of nonlinear partial differential equations for the metric functions. The solutions of the partial differential equations can describe scalarized KN black holes with a nontrivial profile of the scalar field or KN black holes with $\phi=0$.

In the stationary spacetime, two Killing vectors ∂_t and ∂_φ are present, and their combination $\xi=\partial_t+\Omega_H\partial\varphi$, where Ω_H is the angular velocity of the black hole horizon, is both orthogonal to and null at the horizon. Consequently, the surface gravity κ is defined as $\kappa^2=-\left(\nabla_\mu\xi_\nu\right)\left(\nabla^\mu\xi^\nu\right)/2$, and it is related to the Hawking temperature T_H as given in [80]

$$T_H=\frac{\kappa}{2\pi}=\frac{1}{4\pi r_H}e^{F_0(r_H,\theta)-F_1(r_H,\theta)}. \tag{2.10}$$

In the EMS model, the black hole entropy is expressed as $S=A_H/4$, where the area of the horizon A_H is given by

$$A_H=2\pi r_H^2\int_0^\pi d\theta\sin\theta e^{F_1(r_H,\theta)+F_2(r_H,\theta)}. \tag{2.11}$$

Various physical quantities, such as the black hole mass M, the black hole charge Q, the black hole angular momentum J, the electrostatic potential Φ and the horizon angular

JHEP10(2023)076

velocity Ω_H, can be determined by studying the asymptotic behavior of the metric functions at the event horizon and spatial infinity [80, 81],

$$\begin{aligned} &A_t|_{r=r_H} \sim 0, && W|_{r=r_H} \sim r_H^2 \Omega_H, \\ &A_t|_{r=\infty} \sim \Phi - \frac{Q}{r}, && W|_{r=\infty} \sim \frac{2J}{r}, \qquad e^{2F_0} N\Big|_{r=\infty} \sim 1 - \frac{2M}{r}. \end{aligned} \tag{2.12}$$

Moreover, these physical quantities are related by the Smarr relation [63, 80, 82]

$$M = 2T_H S + 2\Omega_H J + \Phi Q, \tag{2.13}$$

which enables us to assess the accuracy of our numerical black hole solutions.

2.3 Light ring

Light rings are null circular geodesics in the black hole spacetime and plays a crucial role in strong gravitational lensing and in the formation of black hole images. For simplicity, we focus on light rings on the equatorial plane. On the equatorial plane, the motion of photons is described by the Lagrangian

$$\mathcal{L} = -\frac{e^{2F_0} N \dot{t}^2}{2} + \frac{e^{2F_1}}{2N} \dot{r}^2 + \frac{e^{2F_2} r^2}{2} \left(\dot{\phi} - \frac{W}{r^2} \dot{t} \right)^2, \tag{2.14}$$

where dots denote derivatives with respect to an affine parameter λ. The conserved energy E and angular momentum L of photons, associated with the Killing vectors ∂_t and ∂_φ, respectively, are expressed as

$$\begin{aligned} E &= \left(e^{2F_0} N - e^{2F_2} \frac{W^2}{r^2} \right) \dot{t} + e^{2F_2} W \dot{\varphi}, \\ L &= e^{2F_2} \left(r^2 \dot{\phi} - W \dot{t} \right). \end{aligned} \tag{2.15}$$

By substituting eq. (2.15) into eq. (2.14), the constancy of the Lagrangian $\mathcal{L} = 0$ reduces to the radial equation for photons,

$$\dot{r}^2 + V_{\text{eff}} = 0, \tag{2.16}$$

where $V_{\text{eff}} \leq 0$ for null geodesics. Here, the effective potential is defined as

$$V_{\text{eff}} = L^2 e^{-2F_1} N \left[\frac{e^{-2F_2}}{r^2} - \frac{e^{-2F_0}}{N} \left(\frac{1}{b} - \frac{W}{r^2} \right)^2 \right], \tag{2.17}$$

where $b \equiv L/E$ is the impact parameter. Thus, for a photon with an impact parameter b_c, it would follow a circular orbit at $r = r_c$ if $V_{\text{eff}}(b_c, r_c) = 0$ and $\partial_r V_{\text{eff}}(b_c, r_c) = 0$.

To facilitate further analysis, we can factorize the effective potential V_{eff} as shown in [83],

$$V_{\text{eff}} = -L^2 e^{-2F_1 - 2F_0} \left(\frac{1}{b} - H_+ \right) \left(\frac{1}{b} - H_- \right), \tag{2.18}$$

where

$$H_+ = \frac{\sqrt{e^{2F_0 - 2F_2} N r^2} + W}{r^2}, \quad H_- = -\frac{\sqrt{e^{2F_0 - 2F_2} N r^2} - W}{r^2}. \tag{2.19}$$

JHEP10(2023)076

Notably, the two redefined effective potentials, H_+ and H_-, are independent of the impact parameter and describe prograde and retrograde motion of photons on the equatorial plane, respectively. For a null geodesic, the effective potentials H_+ and H_- must satisfy $H_+ < b^{-1}$ or $H_- > b^{-1}$, where $H_+ \geq H_-$. In particular, a null circular geodesic at $r = r_c$ corresponds to a local extremum of H_+ or H_-, meaning $\partial_r H_+(r_c) = 0$ or $\partial_r H_-(r_c) = 0$. Moreover, $\partial_r^2 H_+(r_c) > 0$ and $\partial_r^2 H_+(r_c) < 0$ indicate stable and unstable prograde light rings, respectively, while $\partial_r^2 H_-(r_c) < 0$ and $\partial_r^2 H_-(r_c) > 0$ correspond to stable and unstable retrograde light rings, respectively. It is worth mentioning that in the static case with $W = 0$, light rings can be solely determined by either H_+ or H_- since $H_+ = -H_-$.

2.4 Numerical scheme

In this paper, we utilize pseudospectral methods to numerically solve the linear partial differential equation (2.3) for zero-modes $\delta\phi(r, \theta)$ and a set of coupled nonlinear partial differential equations for scalarized KN black holes. Pseudospectral methods are a well-established approach for solving partial differential equations [84]. They approximate the exact solution by a finite linear combination of basis functions. Notably, as the number of degrees-of-freedom increases, pseudospectral methods exhibit an exponential convergence rate for well-behaved functions, in contrast to the linear or polynomial convergence of finite difference or finite element methods. Recently, these pseudospectral methods have demonstrated successful applications in searching for black hole solutions [82, 85, 86], as well as computing black hole quasinormal modes [87–89]. For technical details of pseudospectral methods in the context of black hole physics, interested readers can refer to [82].

For the numerical implementation, we introduce a new radial variable given by

$$x = \frac{\sqrt{r^2 - r_H^2} - r_H}{\sqrt{r^2 - r_H^2} + r_H}, \tag{2.20}$$

which allows us to map the event horizon and spatial infinity to $x = -1$ and $x = 1$, respectively. By performing series expansions of the solutions at the event horizon, we obtain the corresponding boundary conditions

$$\partial_x \delta\phi = \partial_x F_0 = \partial_x F_1 = \partial_x F_2 = \partial_x \phi = \partial_x A_\varphi = A_t = W - \Omega_H = 0 \text{ at } x = -1. \tag{2.21}$$

Moreover, due to the flatness at the spatial infinity, we have

$$\delta\phi = F_0 = F_1 = F_2 = \phi = A_\varphi = A_t - \Phi = W = 0 \text{ at } x = 1. \tag{2.22}$$

On the other hand, the regularity on the symmetric axis imposes the conditions

$$\partial_\theta \delta\phi = \partial_\theta F_0 = \partial_\theta F_1 = \partial_\theta F_2 = \partial_\theta \phi = \partial_\theta A_\varphi = \partial_\theta A_t = \partial_\theta W = 0 \text{ at } \theta = 0 \text{and } \pi. \tag{2.23}$$

Since all solutions are symmetric with respect to the equatorial plane, we can restrict the analysis to the upper half domain with $0 \leq \theta \leq \pi/2$, and hence replace the $\theta = \pi$ boundary condition in eq. (2.23) with

$$\partial_\theta \delta\phi = \partial_\theta F_0 = \partial_\theta F_1 = \partial_\theta F_2 = \partial_\theta \phi = \partial_\theta A_\varphi = \partial_\theta A_t = \partial_\theta W = 0 \text{ at } \theta = \pi/2. \tag{2.24}$$

JHEP10(2023)076

Consequently, eqs. (2.21), (2.22), (2.23) and (2.24) serve as boundary conditions for solving the partial differential equations. Additionally, the absence of conical singularities requires $F_1 = F_2$ on the symmetric axis, which can be used to verify our numerical results as well as the Smarr relation [40, 80].

With the compactified radial coordinate x, the functions of interest, which are collectively denoted by $\mathcal{F} = \{F_0, F_1, F_2, W, A_t, A_\varphi, \phi, \delta\phi\}$, can be decomposed into a spectral expansion,

$$\mathcal{F}^{(k)} = \sum_{i=0}^{N_x-1} \sum_{j=0}^{N_\theta-1} \alpha_{ij}^{(k)} T_i(x) \cos(2j\theta) \,. \tag{2.25}$$

Here, N_x and N_θ represent the resolutions in the radial and angular coordinates, respectively, $T_i(x)$ is the Chebyshev polynomial, and $\alpha_{ij}^{(k)}$ are the spectral coefficients. As investigated in [82], it has been noted that the spectral method for obtaining black hole solutions demonstrates exponential convergence as the resolution is increased until reaching a roundoff plateau. In this context, we have conducted tests on our numerical implementation at various resolutions, and our results indeed confirm this exponential convergence. To ensure numerical precision and efficiency, we set $(N_x, N_\theta) = (22, 5)$ and $(N_x, N_\theta) = (42, 8)$ for the subsequent numerical computations of the zero-modes and the metric functions, respectively. To determine $\alpha_{ij}^{(k)}$, we substitute the spectral expansions (2.25) into the partial differential equations and discretize the resulting equations at the Gauss-Chebyshev points. This process reduces the partial differential equations of $\mathcal{F}$ to a finite system of algebraic equations of α_{ij}. We then solve these algebraic equations for α_{ij} by a standard iterative Newton-Raphson method, where the resulting linear system of equations is solved using the built-in command LinearSolve in Mathematica.

3 Numerical results

In this section, we explore the domain of existence for scalarized KN black hole solutions and conduct an analysis of the light ring structure. To facilitate our study, we introduce dimensionless reduced quantities, $q \equiv Q/M$, $\chi \equiv a/M$ and $a_H \equiv A_H/16\pi M^2$. In the pursuit of scalarized KN black holes, we employ the Newton-Raphson algorithm to iteratively refine our solutions until the corrections between two consecutive iterations fall below the threshold of 10^{-10}. Throughout our numerical implementation, we estimate the numerical accuracy of these black hole solutions through two criteria: the absence of conical singularities (i.e., $F_1 = F_2$) and adherence to the Smarr relation (2.13). Our results reveal that these conditions hold true with a numerical error on the order of 10^{-10} when the scalarized KN black hole solutions are sufficiently distant from the critical line. However, as we approach the critical line, the solutions exhibit a numerical error on the order of 10^{-8}.

3.1 Domain of existence

To determine the existence domain of scalarized KN black holes, we adopt a step-by-step approach. Initially, we obtain scalarized black hole solutions along the extreme line of KN black holes by iteratively using the solution from the previous step as the starting values

JHEP10(2023)076

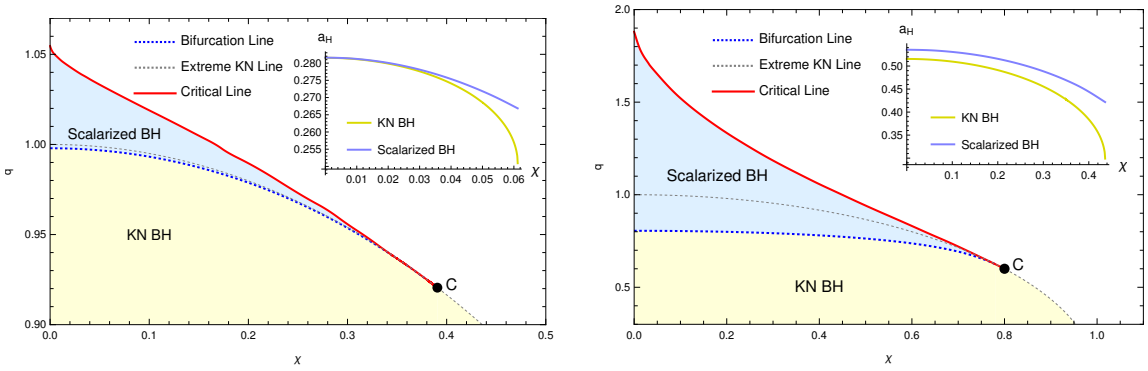

Figure 2. Domain of existence for scalarized KN black holes in the q-χ plane, with $\alpha = 0.8$ (*left*) and $\alpha = 5$ (*right*), depicted by the regions shaded in light blue. The domain of existence is bounded by the bifurcation and critical lines. The blue dashed lines represent the bifurcation lines, indicating the points where scalarized black holes emerge from KN black holes as zero modes. Meanwhile, the red lines indicate critical configurations of scalarized black holes, characterized by a vanishing horizon area while the mass and charge remain finite. Interestingly, as the black hole spin increases, the bifurcation and critical lines approach each other and eventually converge at the critical point C, illustrating the suppressive effect of rotation on scalarization. KN black holes are situated below the extreme lines, marked by dashed gray lines, and coexist with scalarized black holes in the regions lying between the bifurcation and extreme lines. The insets in the left and right panels depict the reduced horizon area as a function of χ for $q = 0.998$ scalarized black holes with $\alpha = 0.8$ and $q = 0.900$ scalarized black holes with $\alpha = 5$, respectively. These insets demonstrate that scalarized black holes are entropically favored in the coexistence regions.

for Newton-Raphson computations at the current step. This procedure starts with the scalarized RN black hole solution, where $q = 1$, and gradually leads to scalarized KN black hole solutions on the extreme line. In each panel of figure 2, the extreme line is comprised of approximately 100 discrete scalarized black hole solutions, serving as the initial solutions for identifying the boundaries of the existence domain. Subsequently, we proceed by varying q to compute scalarized black hole solutions along χ-constant lines until it becomes unfeasible to find additional solutions. More precisely, we initiate this process with the scalarized black hole solutions obtained from the extreme line, systematically scanning solutions with a fixed χ until no further solutions are found within a q-step of 10^{-3}. Consequently, the χ-constant lines spanning between the boundaries consist of roughly 30 scalarized black hole solutions.

In figure 2, the left and right panels present the existence domain of scalarized KN black holes with $\alpha = 0.8$ and $\alpha = 5$, respectively, in the q-χ parameter space. The light blue region represents the domain where scalarized black holes exist, and it is delimited by the bifurcation line and the critical line. The bifurcation lines indicate the threshold where the tachyonic instabilities near the event horizon of scalar-free black holes are strong enough to trigger the formation of scalarized black holes. Remarkably, our numerical findings demonstrate that the bifurcation lines coincide perfectly with the zero-mode lines in the q-χ parameter space. This coincidence is expected since scalarized black hole solutions originate from the bifurcation lines as zero modes. On the other hand, scalarized black hole

JHEP10(2023)076

solutions lying on the critical lines possess a vanishing horizon area, while the black hole mass M and charge Q remain finite.

Figure 2 demonstrates the occurrence of spontaneous scalarization in the EMS model for rotating black holes; however, it is suppressed for high spins. Notably, the bifurcation and critical lines converge and terminate at the critical point C on the extreme line, setting an upper limit on the spin of scalarized black holes. This observation suggests that sufficiently large spin values mitigate tachyonic instabilities, thereby impeding the initiation of spontaneous scalarizations. Moreover, a larger coupling constant α facilitates the scalarization of KN black holes, leading to an expansion of the existence domain for scalarized black holes.

Of particular interest is the coexistence region where scalarized and KN black holes both exist, and this region is delimited by the bifurcation and extreme lines. The inset in each panel displays that scalarized black holes consistently exhibit a greater reduced area of the event horizon when compared to KN black holes. This compelling observation suggests that within the coexistence region, scalarized black holes are entropically favored over scalar-free black holes. Lastly, it is worth noting that scalarized black holes can be overcharged in the parameter region lying between the extremal and critical lines.

3.2 Light ring structure

As discussed earlier, the maxima and minima of H_+ correspond to unstable and stable prograde light rings, respectively, while the maxima and minima of H_- correspond to stable and unstable retrograde light rings, respectively. To study the light ring structure on the equatorial plane, we investigate the extrema of the effective potentials H_+ and H_- for scalarized KN black holes. In the upper panel of figure 3, we present the light ring structure for scalarized black holes with $\alpha = 0.8$ in the q-χ plane, with a zoomed-in inset providing more details. When $\chi = 0$, the threshold points A with $q_A = 1.0463$ and B with $q_B = 1.0492$ determine the structure of light rings (or equivalently, photon spheres in the static case) for scalarized RN black holes. The black lines in the left and right panels of figure 4 represent the effective potentials of scalarized RN black holes at points A and B, respectively. At the threshold point A, the effective potential H_+ (H_-) displays a maximum (minimum) and an inflection point, which splits into a minimum (maximum) and an additional maximum (minimum) for $q > q_A$. Consequently, scalarized RN black holes with $q > q_A$ possess two unstable and one stable light rings. On the other hand, at the threshold point B, there are two potential peaks (well) of the effective potential H_+ (H_-) with the same height (depth). For $q > q_B$, the potential peak (well) at the inner light ring is higher (lower) than the one at the outer ring, indicating that the inner light ring is visible to a distant observer, and thus plays a significant role in determining the optical appearances of luminous matters [68–71]. Accordingly, light rings at the higher (lower) inner potential peak (well) of H_+ (H_-) are referred to as visible inner light rings hereinafter.

As scalarized black holes acquire spin, a single threshold point transforms into two threshold curves, each associated with prograde and retrograde light rings, respectively. In figure 3, the resulting four threshold curves are as follows:

JHEP10(2023)076

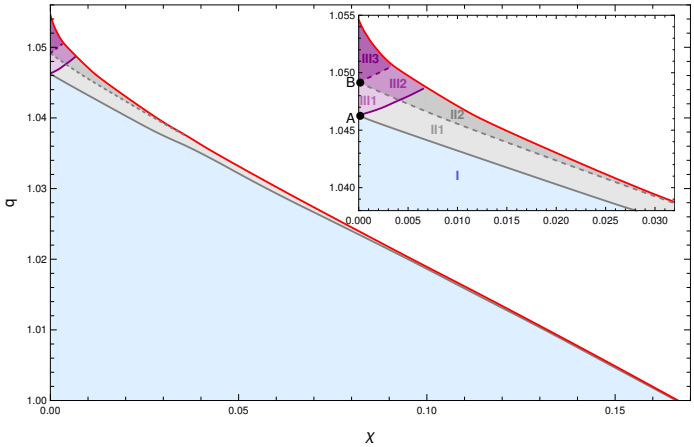

		Prograde Light Ring			Retrograde Light Ring		
		Unstable	Stable	Visible Inner	Unstable	Stable	Visible Inner
Region I	I	1	0	/	1	0	/
Region II	II1	2	1	✘	1	0	/
	II2	2	1	✓	1	0	/
Region III	III1	2	1	✘	2	1	✘
	III2	2	1	✓	2	1	✘
	III3	2	1	✓	2	1	✓

Figure 3. *Upper*: scalarized black holes exhibit distinct light ring structures in various regions of the q-χ plane. The boundaries separating these regions are represented by threshold curves, and the corresponding effective potentials are illustrated in figure 4. Here, we set $\alpha = 0.8$. *Lower*: the table displays the number of unstable and stable light rings for scalarized black holes in the six regions as shown in the upper panel. The table header "Visible Inner" indicates whether photons originating from inner light rings can reach a distant observer.

- The I/II curve, represented by the solid gray line, exhibits a maximum and an inflection point in H_+. The left panel of figure 4 provides a typical example of the effective potentials, depicted by the solid gray lines.
- The II/III curve, shown by the solid purple line, features a minimum and an inflection point in H_-. The left panel of figure 4 illustrates a typical example of the effective potentials, denoted by the solid purple lines.
- The II1/II2 curve, denoted by the dashed gray line, has two potential peaks of H_+ at the same height. The right panel of figure 4 displays a typical example of the effective potentials, represented by the dashed grays.
- The III2/III3 curve, indicated by the dashed purple line, involves two potential wells of H_- with the same depth. The right panel of figure 4 shows a typical example of the effective potentials, depicted by the dashed purple lines.

As a consequence, the four threshold curves partition the domain of existence into six regions, each corresponding to a distinct light ring structure, as depicted in the upper panel of figure 3. The light ring properties in these six regions are presented in the lower

JHEP10(2023)076

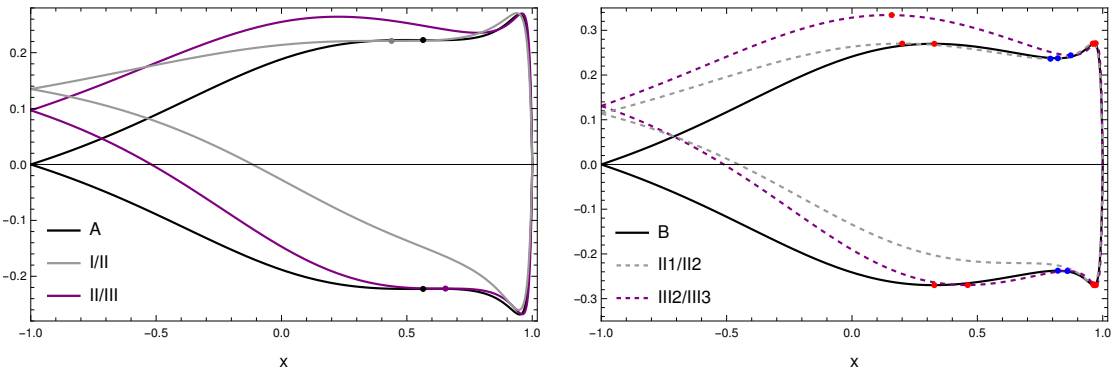

Figure 4. The effective potentials as a function of x for scalarized black holes with $\alpha = 0.8$ on the threshold curves. The upper and lower branches of the effective potentials denotes the prograde potential H_+ and the retrograde potential H_-, respectively. *Left*: the effective potentials are displayed for the black hole with $q = 1.0463$ and $\chi = 0$ at point A, the one with $q = 1.0400$ and $\chi = 0.0202$ on the I/II curve, and the one with $q = 1.0475$ and $\chi = 0.0038$ on the II/III curve. Inflection points are marked with colored dots, which transform into a maximum and a minimum as q increases. *Right*: the effective potentials are shown for the black hole with $q = 1.0492$ and $\chi = 0$ at point B, the one with $q = 1.0475$ and $\chi = 0.0044$ on the II1/II2 curve, and the one with $q = 1.0500$ and $\chi = 0.0021$ on the III2/III3 curve. Unstable and stable light rings are represented by red and blue dots, respectively. The potential peaks or wells at two unstable light rings possess identical height or depth for $H_\pm$ at point B, H_+ on the II1/II2 curve and H_- on the III2/III3 curve.

table of figure 3. Additionally, we showcase the effective potentials of representative black hole solutions in figure 5. Remarkably, our findings indicate that the number of unstable light rings is always one greater than the number of stable ones, consistent with prior observations in [90]. Intriguingly, for a given q, a sufficiently high spin can engender multiple light rings, even from scalarized RN black holes with only one light ring. Lastly, it is worth noting that prograde photons are more likely to possess multiple light rings compared to retrograde photons.

4 Conclusions

This paper first presented our numerical construction of scalarized rotating black hole solutions within the EMS model and explored the parameter regions in which these solutions exist. The EMS model incorporates a non-minimal coupling between the scalar and electromagnetic fields, leading to tachyonic instabilities that can trigger the formation of scalarized KN black holes. Our findings demonstrated that the black hole spin tends to inhibit the spontaneous scalarization of KN black holes, and scalarized KN black holes cease to exist beyond a certain threshold spin. Later, we delved into the light ring structure of scalarized KN black holes. We found that slowly-rotating scalarized black holes with a small electric charge typically possess one unstable prograde and one unstable retrograde light rings. However, as scalarized black holes spin faster, two unstable and one stable prograde light rings can emerge. Additionally, for sufficiently large black hole charge, two unstable and one stable retrograde light rings can also be observed.

JHEP10(2023)076

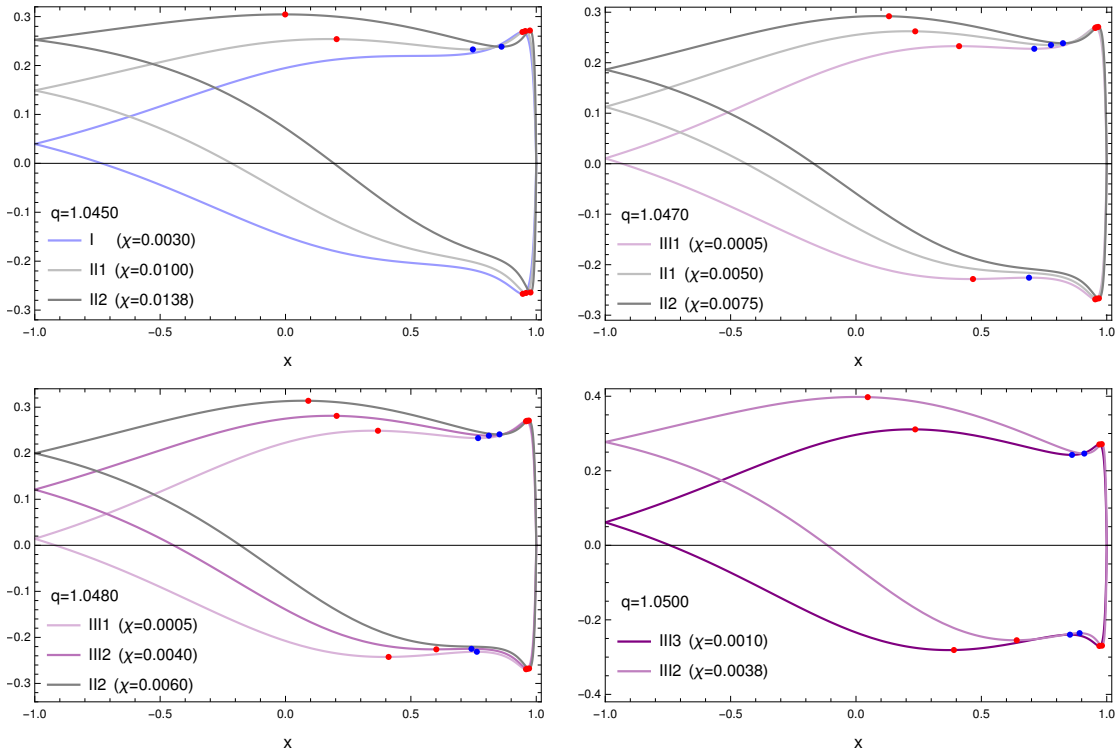

Figure 5. The effective potentials as a function of x for representative scalarized black hole solutions with $\alpha = 0.8$ in the regions characterized by distinct light ring structures. The upper and lower branches of the effective potentials are denoted as the prograde potential H_+ and the retrograde potential H_-, respectively. Red and blue dots represent unstable and stable light rings, respectively.

As previously investigated in [42], it has been established that there exists a critical coupling constant $\alpha = 1/4$, below which scalarized RN black holes cannot exist. Similarly, our numerical computations have not yielded any scalarized KN black hole solutions for values of α below 1/4. This result aligns with expectations, as the presence of black hole spin has a suppressive effect on spontaneous scalarization in KN black holes.

Investigating the existence of scalarized black holes with negative coupling constants α and understanding their formation from scalar-free black holes are promising avenues for future research. Furthermore, this work has shed light on the intricate behavior of scalarized rotating black holes within the EMS model. Future studies may explore the stability of these solutions and investigate their observable signatures, taking advantage of the rich light ring structure they exhibit. Such investigations will further enhance our understanding of rotating black holes with multiple light rings and contribute to the broader field of black hole physics.

Acknowledgments

We are grateful to Yiqian Chen and Qingyu Gan for useful discussions and valuable comments. This work is supported in part by NSFC (Grant No. 12105191, 12275183, 12275184 and 11875196). Houwen Wu is supported by the International Visiting Program for Excellent Young Scholars of Sichuan University.

JHEP10(2023)076

References

[1] LIGO Scientific and Virgo collaborations, *Observation of Gravitational Waves from a Binary Black Hole Merger*, *Phys. Rev. Lett.* **116** (2016) 061102 [arXiv:1602.03837] [INSPIRE].

[2] E. Berti, V. Cardoso, J.A. Gonzalez and U. Sperhake, *Mining information from binary black hole mergers: A Comparison of estimation methods for complex exponentials in noise*, *Phys. Rev. D* **75** (2007) 124017 [gr-qc/0701086] [INSPIRE].

[3] R.H. Price and G. Khanna, *Gravitational wave sources: reflections and echoes*, *Class. Quant. Grav.* **34** (2017) 225005 [arXiv:1702.04833] [INSPIRE].

[4] M. Giesler, M. Isi, M.A. Scheel and S. Teukolsky, *Black Hole Ringdown: The Importance of Overtones*, *Phys. Rev. X* **9** (2019) 041060 [arXiv:1903.08284] [INSPIRE].

[5] Event Horizon Telescope collaboration, *First M87 Event Horizon Telescope Results. IV. Imaging the Central Supermassive Black Hole*, *Astrophys. J. Lett.* **875** (2019) L4 [arXiv:1906.11241] [INSPIRE].

[6] Event Horizon Telescope collaboration, *First M87 Event Horizon Telescope Results. II. Array and Instrumentation*, *Astrophys. J. Lett.* **875** (2019) L2 [arXiv:1906.11239] [INSPIRE].

[7] Event Horizon Telescope collaboration, *First M87 Event Horizon Telescope Results. I. The Shadow of the Supermassive Black Hole*, *Astrophys. J. Lett.* **875** (2019) L1 [arXiv:1906.11238] [INSPIRE].

[8] Event Horizon Telescope collaboration, *First M87 Event Horizon Telescope Results. VI. The Shadow and Mass of the Central Black Hole*, *Astrophys. J. Lett.* **875** (2019) L6 [arXiv:1906.11243] [INSPIRE].

[9] Event Horizon Telescope collaboration, *First M87 Event Horizon Telescope Results. V. Physical Origin of the Asymmetric Ring*, *Astrophys. J. Lett.* **875** (2019) L5 [arXiv:1906.11242] [INSPIRE].

[10] Event Horizon Telescope collaboration, *First M87 Event Horizon Telescope Results. III. Data Processing and Calibration*, *Astrophys. J. Lett.* **875** (2019) L3 [arXiv:1906.11240] [INSPIRE].

[11] Event Horizon Telescope collaboration, *First Sagittarius A* Event Horizon Telescope Results. IV. Variability, Morphology, and Black Hole Mass*, *Astrophys. J. Lett.* **930** (2022) L15 [INSPIRE].

[12] Event Horizon Telescope collaboration, *First Sagittarius A* Event Horizon Telescope Results. V. Testing Astrophysical Models of the Galactic Center Black Hole*, *Astrophys. J. Lett.* **930** (2022) L16 [INSPIRE].

[13] Event Horizon Telescope collaboration, *First Sagittarius A* Event Horizon Telescope Results. II. EHT and Multiwavelength Observations, Data Processing, and Calibration*, *Astrophys. J. Lett.* **930** (2022) L13 [INSPIRE].

JHEP10(2023)076

[14] Event Horizon Telescope collaboration, *First Sagittarius A* Event Horizon Telescope Results. III. Imaging of the Galactic Center Supermassive Black Hole*, *Astrophys. J. Lett.* **930** (2022) L14 [INSPIRE].

[15] Event Horizon Telescope collaboration, *First Sagittarius A* Event Horizon Telescope Results. I. The Shadow of the Supermassive Black Hole in the Center of the Milky Way*, *Astrophys. J. Lett.* **930** (2022) L12 [INSPIRE].

[16] Event Horizon Telescope collaboration, *First Sagittarius A* Event Horizon Telescope Results. VI. Testing the Black Hole Metric*, *Astrophys. J. Lett.* **930** (2022) L17 [INSPIRE].

[17] W. Israel, *Event horizons in static vacuum space-times*, *Phys. Rev.* **164** (1967) 1776 [INSPIRE].

[18] B. Carter, *Axisymmetric Black Hole Has Only Two Degrees of Freedom*, *Phys. Rev. Lett.* **26** (1971) 331 [INSPIRE].

[19] R. Ruffini and J.A. Wheeler, *Introducing the black hole*, *Phys. Today* **24** (1971) 30 [INSPIRE].

[20] M.S. Volkov and D.V. Galtsov, *NonAbelian Einstein Yang-Mills black holes*, *JETP Lett.* **50** (1989) 346 [INSPIRE].

[21] P. Bizon, *Colored black holes*, *Phys. Rev. Lett.* **64** (1990) 2844 [INSPIRE].

[22] B.R. Greene, S.D. Mathur and C.M. O'Neill, *Eluding the no hair conjecture: Black holes in spontaneously broken gauge theories*, *Phys. Rev. D* **47** (1993) 2242 [hep-th/9211007] [INSPIRE].

[23] H. Luckock and I. Moss, *Black holes have skyrmion hair*, *Phys. Lett. B* **176** (1986) 341 [INSPIRE].

[24] S. Droz, M. Heusler and N. Straumann, *New black hole solutions with hair*, *Phys. Lett. B* **268** (1991) 371 [INSPIRE].

[25] P. Kanti et al., *Dilatonic black holes in higher curvature string gravity*, *Phys. Rev. D* **54** (1996) 5049 [hep-th/9511071] [INSPIRE].

[26] S. Mahapatra, S. Priyadarshinee, G.N. Reddy and B. Shukla, *Exact topological charged hairy black holes in AdS Space in D-dimensions*, *Phys. Rev. D* **102** (2020) 024042 [arXiv:2004.00921] [INSPIRE].

[27] S. Priyadarshinee, S. Mahapatra and I. Banerjee, *Analytic topological hairy dyonic black holes and thermodynamics*, *Phys. Rev. D* **104** (2021) 084023 [arXiv:2108.02514] [INSPIRE].

[28] S. Priyadarshinee and S. Mahapatra, *Analytic three-dimensional primary hair charged black holes and thermodynamics*, *Phys. Rev. D* **108** (2023) 044017 [arXiv:2305.09172] [INSPIRE].

[29] R. Ghosh, S. Sk and S. Sarkar, *Hairy black holes: Nonexistence of short hairs and a bound on the light ring size*, *Phys. Rev. D* **108** (2023) L041501 [arXiv:2306.14193] [INSPIRE].

[30] T. Damour and G. Esposito-Farese, *Nonperturbative strong field effects in tensor-scalar theories of gravitation*, *Phys. Rev. Lett.* **70** (1993) 2220 [INSPIRE].

[31] I.Z. Stefanov, S.S. Yazadjiev and M.D. Todorov, *Phases of 4D scalar-tensor black holes coupled to Born-Infeld nonlinear electrodynamics*, *Mod. Phys. Lett. A* **23** (2008) 2915 [arXiv:0708.4141] [INSPIRE].

[32] D.D. Doneva, S.S. Yazadjiev, K.D. Kokkotas and I.Z. Stefanov, *Quasi-normal modes, bifurcations and non-uniqueness of charged scalar-tensor black holes*, *Phys. Rev. D* **82** (2010) 064030 [arXiv:1007.1767] [INSPIRE].

JHEP10(2023)076

[33] V. Cardoso, I.P. Carucci, P. Pani and T.P. Sotiriou, *Matter around Kerr black holes in scalar-tensor theories: scalarization and superradiant instability*, *Phys. Rev. D* **88** (2013) 044056 [arXiv:1305.6936] [INSPIRE].

[34] V. Cardoso, I.P. Carucci, P. Pani and T.P. Sotiriou, *Black holes with surrounding matter in scalar-tensor theories*, *Phys. Rev. Lett.* **111** (2013) 111101 [arXiv:1308.6587] [INSPIRE].

[35] D.D. Doneva and S.S. Yazadjiev, *New Gauss-Bonnet Black Holes with Curvature-Induced Scalarization in Extended Scalar-Tensor Theories*, *Phys. Rev. Lett.* **120** (2018) 131103 [arXiv:1711.01187] [INSPIRE].

[36] H.O. Silva et al., *Spontaneous scalarization of black holes and compact stars from a Gauss-Bonnet coupling*, *Phys. Rev. Lett.* **120** (2018) 131104 [arXiv:1711.02080] [INSPIRE].

[37] G. Antoniou, A. Bakopoulos and P. Kanti, *Evasion of No-Hair Theorems and Novel Black-Hole Solutions in Gauss-Bonnet Theories*, *Phys. Rev. Lett.* **120** (2018) 131102 [arXiv:1711.03390] [INSPIRE].

[38] D.D. Doneva et al., *Charged Gauss-Bonnet black holes with curvature induced scalarization in the extended scalar-tensor theories*, *Phys. Rev. D* **98** (2018) 104056 [arXiv:1809.00844] [INSPIRE].

[39] P.V.P. Cunha, C.A.R. Herdeiro and E. Radu, *Spontaneously Scalarized Kerr Black Holes in Extended Scalar-Tensor-Gauss-Bonnet Gravity*, *Phys. Rev. Lett.* **123** (2019) 011101 [arXiv:1904.09997] [INSPIRE].

[40] C.A.R. Herdeiro et al., *Spin-induced scalarized black holes*, *Phys. Rev. Lett.* **126** (2021) 011103 [arXiv:2009.03904] [INSPIRE].

[41] E. Berti, L.G. Collodel, B. Kleihaus and J. Kunz, *Spin-induced black-hole scalarization in Einstein-scalar-Gauss-Bonnet theory*, *Phys. Rev. Lett.* **126** (2021) 011104 [arXiv:2009.03905] [INSPIRE].

[42] C.A.R. Herdeiro, E. Radu, N. Sanchis-Gual and J.A. Font, *Spontaneous Scalarization of Charged Black Holes*, *Phys. Rev. Lett.* **121** (2018) 101102 [arXiv:1806.05190] [INSPIRE].

[43] P.G.S. Fernandes et al., *Spontaneous Scalarisation of Charged Black Holes: Coupling Dependence and Dynamical Features*, *Class. Quant. Grav.* **36** (2019) 134002 [*Erratum ibid.* **37** (2020) 049501] [arXiv:1902.05079] [INSPIRE].

[44] P.G.S. Fernandes et al., *Charged black holes with axionic-type couplings: Classes of solutions and dynamical scalarization*, *Phys. Rev. D* **100** (2019) 084045 [arXiv:1908.00037] [INSPIRE].

[45] J.L. Blázquez-Salcedo et al., *Einstein-Maxwell-scalar black holes: the hot, the cold and the bald*, *Phys. Lett. B* **806** (2020) 135493 [arXiv:2002.00963] [INSPIRE].

[46] D.-C. Zou and Y.S. Myung, *Scalarized charged black holes with scalar mass term*, *Phys. Rev. D* **100** (2019) 124055 [arXiv:1909.11859] [INSPIRE].

[47] P.G.S. Fernandes, *Einstein-Maxwell-scalar black holes with massive and self-interacting scalar hair*, *Phys. Dark Univ.* **30** (2020) 100716 [arXiv:2003.01045] [INSPIRE].

[48] Y. Peng, *Scalarization of horizonless reflecting stars: neutral scalar fields non-minimally coupled to Maxwell fields*, *Phys. Lett. B* **804** (2020) 135372 [arXiv:1912.11989] [INSPIRE].

[49] Y.S. Myung and D.-C. Zou, *Instability of Reissner-Nordström black hole in Einstein-Maxwell-scalar theory*, *Eur. Phys. J. C* **79** (2019) 273 [arXiv:1808.02609] [INSPIRE].

JHEP10(2023)076

[50] Y.S. Myung and D.-C. Zou, *Stability of scalarized charged black holes in the Einstein-Maxwell-Scalar theory*, *Eur. Phys. J. C* **79** (2019) 641 [arXiv:1904.09864] [INSPIRE].

[51] D.-C. Zou and Y.S. Myung, *Radial perturbations of the scalarized black holes in Einstein-Maxwell-conformally coupled scalar theory*, *Phys. Rev. D* **102** (2020) 064011 [arXiv:2005.06677] [INSPIRE].

[52] Y.S. Myung and D.-C. Zou, *Onset of rotating scalarized black holes in Einstein-Chern-Simons-Scalar theory*, *Phys. Lett. B* **814** (2021) 136081 [arXiv:2012.02375] [INSPIRE].

[53] Z.-F. Mai and R.-Q. Yang, *Stability analysis of a charged black hole with a nonlinear complex scalar field*, *Phys. Rev. D* **104** (2021) 044008 [arXiv:2101.00026] [INSPIRE].

[54] D. Astefanesei, C. Herdeiro, J. Oliveira and E. Radu, *Higher dimensional black hole scalarization*, *JHEP* **09** (2020) 186 [arXiv:2007.04153] [INSPIRE].

[55] Y.S. Myung and D.-C. Zou, *Quasinormal modes of scalarized black holes in the Einstein-Maxwell-Scalar theory*, *Phys. Lett. B* **790** (2019) 400 [arXiv:1812.03604] [INSPIRE].

[56] J. Luis Blázquez-Salcedo et al., *Quasinormal modes of hot, cold and bald Einstein-Maxwell-scalar black holes*, *Eur. Phys. J. C* **81** (2021) 155 [arXiv:2008.11744] [INSPIRE].

[57] Y.S. Myung and D.-C. Zou, *Scalarized charged black holes in the Einstein-Maxwell-Scalar theory with two* U(1) *fields*, *Phys. Lett. B* **811** (2020) 135905 [arXiv:2009.05193] [INSPIRE].

[58] Y.S. Myung and D.-C. Zou, *Scalarized black holes in the Einstein-Maxwell-scalar theory with a quasitopological term*, *Phys. Rev. D* **103** (2021) 024010 [arXiv:2011.09665] [INSPIRE].

[59] H. Guo, X.-M. Kuang, E. Papantonopoulos and B. Wang, *Horizon curvature and spacetime structure influences on black hole scalarization*, *Eur. Phys. J. C* **81** (2021) 842 [arXiv:2012.11844] [INSPIRE].

[60] Y. Brihaye, B. Hartmann, N.P. Aprile and J. Urrestilla, *Scalarization of asymptotically anti-de Sitter black holes with applications to holographic phase transitions*, *Phys. Rev. D* **101** (2020) 124016 [arXiv:1911.01950] [INSPIRE].

[61] Y. Brihaye, C. Herdeiro and E. Radu, *Black Hole Spontaneous Scalarisation with a Positive Cosmological Constant*, *Phys. Lett. B* **802** (2020) 135269 [arXiv:1910.05286] [INSPIRE].

[62] C.-Y. Zhang et al., *Dynamical charged black hole spontaneous scalarization in anti-de Sitter spacetimes*, *Phys. Rev. D* **104** (2021) 084089 [arXiv:2103.13599] [INSPIRE].

[63] G. Guo, P. Wang, H. Wu and H. Yang, *Scalarized Einstein-Maxwell-scalar black holes in anti-de Sitter spacetime*, *Eur. Phys. J. C* **81** (2021) 864 [arXiv:2102.04015] [INSPIRE].

[64] Q. Chen et al., *Nonlinear dynamics of hot, cold and bald Einstein-Maxwell-scalar black holes in AdS spacetime*, arXiv:2307.03060 [INSPIRE].

[65] C.-Y. Zhang et al., *Critical Phenomena in Dynamical Scalarization of Charged Black Holes*, *Phys. Rev. Lett.* **128** (2022) 161105 [arXiv:2112.07455] [INSPIRE].

[66] C.-Y. Zhang et al., *Dynamical transitions in scalarization and descalarization through black hole accretion*, *Phys. Rev. D* **106** (2022) L061501 [arXiv:2204.09260] [INSPIRE].

[67] J.-Y. Jiang et al., *Type I critical dynamical scalarization and descalarization in Einstein-Maxwell-scalar theory*, arXiv:2306.10371 [INSPIRE].

JHEP10(2023)076

[68] Q. Gan, P. Wang, H. Wu and H. Yang, *Photon spheres and spherical accretion image of a hairy black hole*, *Phys. Rev. D* **104** (2021) 024003 [arXiv:2104.08703] [INSPIRE].

[69] Q. Gan, P. Wang, H. Wu and H. Yang, *Photon ring and observational appearance of a hairy black hole*, *Phys. Rev. D* **104** (2021) 044049 [arXiv:2105.11770] [INSPIRE].

[70] G. Guo, X. Jiang, P. Wang and H. Wu, *Gravitational lensing by black holes with multiple photon spheres*, *Phys. Rev. D* **105** (2022) 124064 [arXiv:2204.13948] [INSPIRE].

[71] Y. Chen et al., *Appearance of an infalling star in black holes with multiple photon spheres*, *Sci. China Phys. Mech. Astron.* **65** (2022) 120412 [arXiv:2206.13705] [INSPIRE].

[72] V. Cardoso et al., *Light rings as observational evidence for event horizons: long-lived modes, ergoregions and nonlinear instabilities of ultracompact objects*, *Phys. Rev. D* **90** (2014) 044069 [arXiv:1406.5510] [INSPIRE].

[73] J. Keir, *Slowly decaying waves on spherically symmetric spacetimes and ultracompact neutron stars*, *Class. Quant. Grav.* **33** (2016) 135009 [arXiv:1404.7036] [INSPIRE].

[74] M. Guo, Z. Zhong, J. Wang and S. Gao, *Light rings and long-lived modes in quasiblack hole spacetimes*, *Phys. Rev. D* **105** (2022) 024049 [arXiv:2108.08967] [INSPIRE].

[75] G. Guo, P. Wang, H. Wu and H. Yang, *Quasinormal modes of black holes with multiple photon spheres*, *JHEP* **06** (2022) 060 [arXiv:2112.14133] [INSPIRE].

[76] G. Guo, P. Wang, H. Wu and H. Yang, *Echoes from hairy black holes*, *JHEP* **06** (2022) 073 [arXiv:2204.00982] [INSPIRE].

[77] G. Guo, P. Wang, H. Wu and H. Yang, *Superradiance instabilities of charged black holes in Einstein-Maxwell-scalar theory*, *JHEP* **07** (2023) 070 [arXiv:2301.06483] [INSPIRE].

[78] G. Guo et al., *Black holes with multiple photon spheres*, *Phys. Rev. D* **107** (2023) 124037 [arXiv:2212.12901] [INSPIRE].

[79] M.-Y. Lai, Y.S. Myung, R.-H. Yue and D.-C. Zou, *Spin-charge induced spontaneous scalarization of Kerr-Newman black holes*, *Phys. Rev. D* **106** (2022) 084043 [arXiv:2208.11849] [INSPIRE].

[80] C. Herdeiro and E. Radu, *Construction and physical properties of Kerr black holes with scalar hair*, *Class. Quant. Grav.* **32** (2015) 144001 [arXiv:1501.04319] [INSPIRE].

[81] J.F.M. Delgado, C.A.R. Herdeiro, E. Radu and H. Runarsson, *Kerr-Newman black holes with scalar hair*, *Phys. Lett. B* **761** (2016) 234 [arXiv:1608.00631] [INSPIRE].

[82] P.G.S. Fernandes and D.J. Mulryne, *A new approach and code for spinning black holes in modified gravity*, *Class. Quant. Grav.* **40** (2023) 165001 [arXiv:2212.07293] [INSPIRE].

[83] P.V.P. Cunha et al., *Chaotic lensing around boson stars and Kerr black holes with scalar hair*, *Phys. Rev. D* **94** (2016) 104023 [arXiv:1609.01340] [INSPIRE].

[84] J.P. Boyd, *Chebyshev and Fourier spectral methods*, Courier Corporation (2001).

[85] M.-Y. Lai, D.-C. Zou, R.-H. Yue and Y.S. Myung, *Nonlinearly scalarized rotating black holes in Einstein-scalar-Gauss-Bonnet theory*, *Phys. Rev. D* **108** (2023) 084007 [arXiv:2304.08012] [INSPIRE].

[86] C. Burrage, P.G.S. Fernandes, R. Brito and V. Cardoso, *Spinning black holes with axion hair*, *Class. Quant. Grav.* **40** (2023) 205021 [arXiv:2306.03662] [INSPIRE].

JHEP10(2023)076

[87] A. Jansen, *Overdamped modes in Schwarzschild-de Sitter and a Mathematica package for the numerical computation of quasinormal modes*, *Eur. Phys. J. Plus* **132** (2017) 546 [arXiv:1709.09178] [INSPIRE].

[88] Q. Gan, G. Guo, P. Wang and H. Wu, *Strong cosmic censorship for a scalar field in a Born-Infeld-de Sitter black hole*, *Phys. Rev. D* **100** (2019) 124009 [arXiv:1907.04466] [INSPIRE].

[89] A.K.-W. Chung, P. Wagle and N. Yunes, *Spectral method for the gravitational perturbations of black holes: Schwarzschild background case*, *Phys. Rev. D* **107** (2023) 124032 [arXiv:2302.11624] [INSPIRE].

[90] P.V.P. Cunha and C.A.R. Herdeiro, *Stationary black holes and light rings*, *Phys. Rev. Lett.* **124** (2020) 181101 [arXiv:2003.06445] [INSPIRE].

JHEP10(2023)076